

Emergent Polar Metal Phase in a Van der Waals Mott Magnet

Shiyu Deng,^{1,2,*} Matthew J. Coak,³ Charles R. S. Haines,⁴ Hayrullo Hamidov,^{1,5} Giulio I. Lampronti,⁶ David M. Jarvis,^{1,2} Xiaotian Zhang,¹ Cheng Liu,¹ Dominik Daisenberger,⁷ Mark R. Warren,⁷ Thomas C Hansen,² Stefan Klotz,⁸ Chaebin Kim,⁹ Pengtao Yang,^{10,11} Bosen Wang,^{10,11} Jinguang Cheng,^{10,11} Je-Geun Park,⁹ Andrew R. Wildes,² and Siddharth S Saxena^{1,12,†}

¹*Cavendish Laboratory, University of Cambridge,
J.J. Thomson Avenue, Cambridge, CB3 0HE, UK*

²*Institut Laue-Langevin, 71 Avenue des Martyrs, 38000 Grenoble, France*

³*School of Physics and Astronomy, University of Birmingham,
Edgbaston, Birmingham B15 2TT, United Kingdom*

⁴*Physics, University of East Anglia, Norwich NR4 7TJ, United Kingdom*

⁵*Navoi State University of Mining and Technologies, 72 M. Tarobiy Street, Navoi 210100, Uzbekistan*

⁶*Department of Earth Sciences, University of Cambridge,
Downing Street, Cambridge CB2 3EQ, United Kingdom*

⁷*Diamond Light Source, Harwell Science and Innovation Campus, Didcot, OX11 0DE, United Kingdom*

⁸*Sorbonne Universite, IMPMC, CNRS, UMR 7590, 4 Place Jussieu, 75252 Paris, France*

⁹*Department of Physics and Astronomy, Seoul National University, Seoul 08826, Republic of Korea*

¹⁰*Beijing National Laboratory for Condensed Matter Physics and Institute of Physics,
Chinese Academy of Sciences, Beijing 100190, China*

¹¹*School of Physical Sciences, University of Chinese Academy of Sciences, Beijing 100190, China*

¹²*British Management University Tashkent, 35 Mirza Bobur Street, Tashkent, Uzbekistan*

(Dated: January 24, 2025)

We report the emergence of a polar metal phase in layered van der Waals compound FePSe₃. This Mott insulator with antiferromagnetic order offers a unique opportunity to fully tune an insulator into a polar metal state with pressure, without doping-induced disorder or impurities. Our synchrotron and neutron diffraction data unambiguously show a structural transition and loss of the inversion symmetry. We also observed the suppression of magnetic ordering and an insulator-to-metal transition correspondent with this structural transformation. The loss of the inversion symmetry combined with the pressure-induced metallicity in FePSe₃ offers a new platform to investigate polar metallicity at accessible pressures. Moreover, the high-pressure metallic phase shows unconventional resistivity deviating from the Fermi-liquid description, close to the magnetic critical transition pressure at sufficiently low temperatures, which strongly suggests underlying quantum criticality. Our work not only explores the comprehensive temperature-pressure phase diagram of FePSe₃ but also provides insights for further investigation of van der Waals strongly correlated magnetic compounds.

I. INTRODUCTION

The study of layered van der Waals (vdW) compounds has become increasingly popular since the revolutionary discovery of graphene [1]. Magnetic vdW materials form a particular class of these compounds. In their atomically thin versions, they have attracted particular attention for potential applications in spintronics and magneto-optics [2, 3]. They also offer an excellent platform for studying strongly correlated electrons in low dimensions.

Many vdW magnets are also insulating, but undergo an insulator-to-metal transition (IMT) under the application of pressure [3, 4]. This makes them conceptually similar to the parent compound of cuprates, in that they are both insulating two-dimensional (2D) antiferromagnets. In cuprates, varying stoichiometry drives an insulator to a ‘strange metal’, and eventually superconducting

phase [5, 6]. Varying the pressure applied to layered vdW compounds offers a cleaner and more controllable way to tune physical properties than varying stoichiometry, thus providing great insight into understanding the underlying causes for an IMT and potentially for superconductivity and novel metallicity [7–9].

One intriguing family is the transition metal chalcogenophosphates $TMPX_3$ ($TM = \text{Mn, Fe, Co, Ni, etc.}, X = \text{S, Se}$). These insulating compounds are antiferromagnets at ambient pressure, with the magnetic TM^{2+} ions forming a honeycomb structure within the vdW layers [10–12]. Previous studies have revealed pressure-induced transitions in transport properties from insulating to metallic, and, in some cases, even to superconducting states [4, 13–18]. However, the critical underlying structural transitions remain elusive, prohibiting further investigation and engineering of this compound family.

Crystalline structure and symmetry transitions can be observed by synchrotron diffraction [4, 15, 19, 20] or Raman spectroscopy [21–24]. Magnetic structures can be characterized by neutron diffraction [12]. Nevertheless, we note that the lack of the control of hydrostatic pres-

* Email: denges@ill.fr

† Email: sss21@cam.ac.uk

sure conditions upon these vdW compounds has led to contradictory results and care must be taken in interpreting observed data, as demonstrated in this work and earlier studies [20, 25]. Comprehensive investigations are therefore essential to resolve the pressure-induced physics of these materials. We selected FePSe₃ as the focus of this work, which was recently reported to exhibit superconductivity at approximately 2.5 K and 9.0 GPa [13].

At ambient pressure, the crystal structure of FePSe₃ consists of two layers of Se on a triangular lattice, sandwiching one layer of Fe on a honeycomb lattice, with P₂ dimers located at the centre of each Fe-hexagon [10]. Both P₂ dimers and Fe ions are octahedrally coordinated with neighboring Se. The distances between the nearest-neighbor Fe sites are equal, resulting in a $C3$ rotation symmetry. The layers stack in an $ABCABC$ sequence, with Fe and P₂ aligned along axes parallel to the c -axis, which is normal to the neighboring vdW layers. FePSe₃ crystallizes in a centrosymmetric rhombohedral space group $R\bar{3}$. Below the reported T_N of 108 ~ 119 K, it orders antiferromagnetically with a propagation vector of $[\frac{1}{2}, 0, \pm\frac{1}{2}]$ and spin moments aligned parallel to the c -axis [12, 26].

In this article, we present a multi-probe study of FePSe₃, combining synchrotron and neutron diffraction with resistivity measurements to investigate the effect of hydrostatic pressure on the crystalline structure, magnetic ordering, and electronic transport properties. We combine our results into a detailed phase diagram and discuss the emergent polar metal phase intrinsically related to the loss of inversion symmetry. We also discuss the resistivity's deviation from Fermi-liquid behavior, close to the antiferromagnetic critical transition pressure at sufficiently low temperatures.

II. METHODS

A. Sample Synthesis and Characterisation

FePSe₃ samples were synthesized via two synthesis routes. Both routes had starting materials sealed in quartz tubes that had been cleaned by an acid etching followed by rinsing with demineralized water. All starting materials were of 99.99% purity. Powder samples, used for x-ray and neutron diffraction, were made using a solid-state reaction. This route was used to minimize preferred orientation, known to occur when grinding single crystals due to the vdW nature of the compound. An equivalent of 2 g of starting materials were sealed in quartz tubes, with stoichiometric quantities of Fe and Se. The P content was 10% larger than stoichiometric, with the excess included to account for possible impurity phases. The tubes were sealed containing a pressure of 5 torr of argon. The tubes were then placed in a horizontal two-zone furnace with the starting materials in zone 1. The zones were independently heated to follow the temperature protocol listed in Table I. The protocol

prevented vapour transport as zone 1 was always cooler than zone 2.

The two-zone furnace was also used to synthesize single crystals of FePSe₃. Equivalent of 1 g of starting material, consisting of stoichiometric quantities of Fe, P and Se, were placed in quartz tubes. A small amount of iodine (0.05 g) was included to facilitate vapour transport. The tubes were then sealed under vacuum and loaded in the furnace. The temperature protocol is also listed in Table I. Zone 2 was colder than zone 1 and the crystals grew in zone 2 via a vapour transport mechanism. The crystals were recovered at the end of the synthesis.

TABLE I. Temperature protocols used to synthesize the powder and single crystal samples of FePSe₃.

| | Zone 1 (°C) | Zone 2 (°C) | Duration (h) |
|-----------------|-------------|-------------|--------------|
| Powders | 25 → 650 | 25 → 670 | 6 |
| | 650 | 670 | 168 |
| | 650 → 25 | 670 → 300 | free cooling |
| Single Crystals | 25 → 750 | 25 → 720 | 6 |
| | 750 | 720 | 168 |
| | 750 → 500 | 720 → 450 | 48 |
| | 500 → 150 | 450 → 120 | 6 |
| | 150 → 25 | 120 → 25 | free cooling |

B. Synchrotron Diffraction under Pressure

Powder diffraction data were collected at room temperature on the Extreme Conditions beamline (I15) at Diamond Light Source, UK. An incidence X-ray beam with focused spot size 30 μm and wavelength 0.4246 Å (equivalently to $E = 29.2$ keV) was used to collect the diffraction patterns. A MAR345 area detector was used to record the diffraction pattern with an exposure time of 120 seconds for each scan at a distinctive pressure value. The instrument parameters were calibrated with LaB₆. The data were initially processed using the data analysis software DAWN – II [27]. Further, Le Bail and Rietveld refinements were performed using GSAS – II [28].

Single-crystal diffraction data were collected at room temperature on the Small Molecule Single Crystal Diffraction beamline (I19-2) [29] at Diamond Light Source, UK. Samples were manually reduced to a thickness of about 10 μm and squares of side length 80 μm . The plate-like sample thus had the $c \parallel c^*$ axis, pointing perpendicular to the crystal planes. The sample was laid flat on an anvil. Thus, c^* was parallel to the anvil axis and close to the direction of the incident synchrotron beam. The experimental geometry is comprehensively described in the Supplemental Material (SM) [30]. An incident beam of wavelength 0.4859 Å was used and diffraction data were collected while the crystal rotated in a standard configuration with a Dectric Pila-

tus 300 K detector. The data were then analyzed using *CrysAlis Pro* [31].

Diamond anvil cells (DAC) with rhenium gaskets were used for both powder and single-crystal samples. The culet size of a DAC was approximately 400 μm . A hole was drilled through a rhenium gasket of a diameter less than half that of the culets. The gasket hole contained the FePSe_3 sample, and some small ruby crystals used as a pressure gauge. Two DACs were prepared for powder diffraction. One was loaded with helium gas serving as the pressure-transmitting medium (PTM). The other was packed with powder samples, without a PTM, to explore the influence of the presence of a pressure medium. For single crystal experiments, only one DAC with a helium gas PTM was prepared.

Pressure was applied using a gas-loading membrane system. The generated pressure inside the sample space was determined by optical measurement of the characteristic R_1 fluorescence peak of ruby [32, 33]. The peak position was measured before and after data collection at each pressure point and the average value was taken as the estimated pressure during the measurement. The uncertainties in the pressure values were estimated to be approximately ± 0.1 GPa.

Diffraction peaks from the DAC were identified by fitting the known diamond unit cell and were removed for subsequent treatment. Powder-like diffraction rings from the rhenium gasket were also identified and excluded from refinements. Details of pressure determination, sample data reduction and analysis are in the SM [30].

C. Neutron Powder Diffraction under Pressure

Powder neutron diffraction patterns were collected on the D20 instrument [34] at the Institut Laue-Langevin, France [35], in a comparable manner to our previous study on FePS_3 [36]. The neutron wavelength was 2.42 Å, set via a graphite monochromator. Data were collected using a Paris-Edinburgh type pressure cell press [37] with double-toroidal sintered diamond anvils [38].

Powder samples from the same batch used in the synchrotron powder measurements were used for this experiment. The powder was packed into the two halves of a Ti/Zr null matrix spherical gasket [39] and then placed between the anvils. A 4:1 deuterated methanol/ethanol mixture served as a hydrostatic pressure medium. No pressure gauge was employed, as the pressure dependence of the sample's lattice parameters (at room temperature) was taken from the synchrotron diffraction results. The pressure was determined by refining the neutron diffraction patterns and extracting lattice parameters, which were then matched to the synchrotron data. Typical uncertainty on pressure values was estimated to be ± 0.3 GPa. All pressure changes were made at temperatures where the pressure medium was known to be in its liquid phase [40].

Table II summarizes the scans for the different pressures taken at high- (HT) and low-temperature (LT). At HT, data were collected with 60-minute count times at 300, 300, 245 and 300 K for pressure values of 0, 1.2, 4.1 and 8.3 GPa, respectively. Subsequently, the cell was rapidly cooled to 80 K under constant load by being immersed in liquid nitrogen. At the highest pressure, the cell was subsequently cooled from 80 to 5 K using a closed cycle cryocooler and further cooled to 1.6 K by immersing the cell into liquid ^4He and pumping on it.

TABLE II. Key scans of magnetic scattering data used in the main text for exploring the magnetic properties evolution in powder samples of FePSe_3 .

| Pressure (GPa) | HT | | LT | |
|-------------------|-------|------------|-------|------------|
| | T (K) | Count Time | T (K) | Count Time |
| 0 | 300 | 60 min | – | – |
| 1.2 | 300 | 60 min | 80 | 8×15 min |
| 4.1 | 245 | 60 min | 80 | 8×15 min |
| 8.3 | 300 | 60 min | 1.6 | 8×30 min |

The raw diffraction data had a broad, diffuse background due to the pressure environment and liquid pressure medium. The background was estimated by manually specifying background points away from any diffraction peaks and fitting a smooth Chebychev polynomial through them to subtract from the raw data. All intensities are normalized to a monitor placed in the incident beam. The resulting data were then refined using the Rietveld method as implemented in software *GSAS-II* [28] and *FullProf* [41]. More details on data processing can be found in the SM [30].

D. Resistivity Measurement with Cubic Anvil Cell

The resistivity of a FePSe_3 single crystal sample, from the same batch used for synchrotron diffraction, was measured under various pressures at the Cubic Anvil Cell (CAC) station of Synergetic Extreme Condition User Facility (SECUF), China [42]. The sample was prepared with dimensions 0.23 mm in length (l), 0.22 mm in width (w) and 0.01 mm in height (h). A standard four-probe method was used for resistivity measurements under high pressure. Silver paste (DuPont 4929N) was used to glue gold wires, 20 μm in diameter, to the sample. The resistance (R) of the sample was measured, and the intrinsic resistivity ρ was calculated using the formula, $\rho = R * (w \cdot h) / l$.

The sample was placed inside a Teflon capsule filled with glycerol PTM before being loaded into a CAC. The three-axis compression geometry together with the adoption of liquid PTM ensured an excellent pressure homogeneity. The pressure values in a CAC were estimated from a pressure-loading force calibration curve pre-determined at room temperature. Temperature-

dependent measurements from 300 to 1.6 K were performed using a liquid ^4He cryostat with a 9 T superconducting magnet. A helium exchange gas was used to equilibrate the temperature of a CAC. A thermometer was inserted inside a CAC to keep good thermal contact. Details about assembling samples and calibrating the pressure of a CAC can be found in Ref. [43].

At the lowest pressure point (6.0 GPa), where the sample was expected to be an insulator, two methods were used to measure R . From 300 to 215 K, R was measured using a Lake Shore Model 372 in alternating current (AC) mode with a current of 10^{-7} A at a frequency of 13.7 Hz. From 215 K down to the base temperature 1.6 K, data were collected with a Keithley 2400 and 2182 in direct current (DC) mode with an average current of 10^{-7} A. For higher pressure points, where the sample was expected to be a metal, the data were collected using a Keithley 2400 and 2182 in DC mode with an average current of 10^{-5} A for 7.0 and 8.0 GPa, and 10^{-4} A for 10.0, 12.0 and 13.5 GPa from 300 to 1.6 K.

III. RESULTS

A. Synchrotron Diffraction and Crystalline Structures

The powder diffraction rings of FePSe_3 loaded in helium gas as the PTM showed no significant intensity variation about the Debye-Scherrer cone, indicating that our sample loading procedure was free from strong preferred orientation. The details and subsequent data reductions converting the original diffraction rings into integrated diffraction intensities as a function of 2θ are given in the SM [30].

Fig. 1 (a) presents an evolution of the post-processed powder diffraction patterns across a range of pressures from 0.7 to 34.1 GPa. The integrated intensities are normalized to the maximum intensity for each pressure point. All datasets are shifted vertically by an offset proportional to the pressure value.

The data show a dramatic shift in the 2θ position of a number of peaks between 7.6 and 8.1 GPa which indicates a distinct phase transition. The transition is sharp with little evidence of phase co-existence. There is no peak broadening associated with the transition, suggesting that a single-phase model with minimal distortion may be used to determine the crystal structure of the high-pressure phase. No further phase transition was evident up to the highest measured pressure. The low- and high-pressure phases will subsequently be referred to as LP and HP respectively. Data assigned to these two phases are plotted in blue and orange in Fig. 1 (a) for a straightforward comparison.

Powder diffraction measured in the absence of a PTM showed similar patterns (see SM [30]). No peak broadening was observed at any pressure. A number of new peaks started to appear at 9.6 GPa marking the onset of the

phase transition. Data above 16.3 GPa showed peaks consistent with a pure HP phase. Diffraction patterns between these two pressures could be fitted with both LP and HP phases. The relative weight factors evolve smoothly throughout this wide two-phase co-existence region.

The LP Bragg peak at the lowest 2θ is indexed in the refinement as 003, as marked in Fig. 1 (a). It is reasonable to assume that the crystal structure does not undergo a substantial reconstruction during the transition from LP to HP. Consequently, the position of this peak can be assumed to be due to the change of the interplanar distance at all pressures. The peak undergoes a drastic change at the phase transition, indicating that the interplanar spacing collapses at the LP-HP transition.

The LP data with helium as the PTM were analyzed using the ambient pressure structure model, which had the hexagonal $R\bar{3}$ space group [11]. The refined lattice parameters at the lowest pressure point (0.7 GPa) were determined to be $a = b = 6.238(2)$ Å and $c = 19.49(1)$ Å, which are in reasonable agreement with the literature values at ambient pressure ($a = b = 6.265(6)$ Å, $c = 19.80(2)$ Å, and $\gamma = 120^\circ$) assuming no substantial changes. The HP data were analyzed using the structural model we obtained from our single-crystal synchrotron studies.

In the single-crystal experiment, we collected high-quality diffraction data from 1.4 to 28.0 GPa. Slices of the (hhl) scattering plane exhibit strong-intensity peaks which are indexed as $3\bar{3}l$ and $33l$ where $l = 0, \pm 3$, as shown in Fig. 1 (b). The slices are plotted to scale in Å $^{-1}$. The intensity of the peaks is consistent with the structure factor analysis. The separation between reflection index points peaks along the $[001]$ and $[1\bar{1}0]$ directions can unambiguously reflect the changes of the inter- and intraplanar lattice parameters, respectively. An abrupt increase in separation along the $[001]$ direction is clearly seen from 6.7 to 7.8 GPa (highlighted with yellow color blocks), while changes along the $[1\bar{1}0]$ direction remain negligible throughout the entire pressure range. This observation in the raw data, independent of any structural model, provides definitive and model-independent proof of the interplanar collapse with applied hydrostatic pressure in FePSe_3 .

The lattice parameters were initially refined based on indexed reflections. We used the ambient-pressure lattice parameters of LP as the starting point to refine the cell at the lowest pressure (1.4 GPa). No space group symmetry was forced on the refinement at this step. The well-indexed reflection peaks and refined parameters ($a = 6.185(4)$ Å, $b = 6.176(3)$ Å, $c = 18.89(3)$ Å, $\alpha = 90.28(1)^\circ$, $\beta = 89.90(1)^\circ$ and $\gamma = 119.99(7)^\circ$) are consistent with the $R\bar{3}$ symmetry of LP with tolerable deviations. We consistently refined the lattice parameters for all pressures using the cell parameters at the previous pressure point. The results are summarized in the SM [30].

Fig. 1 (c) summarizes the relative changes of lattice

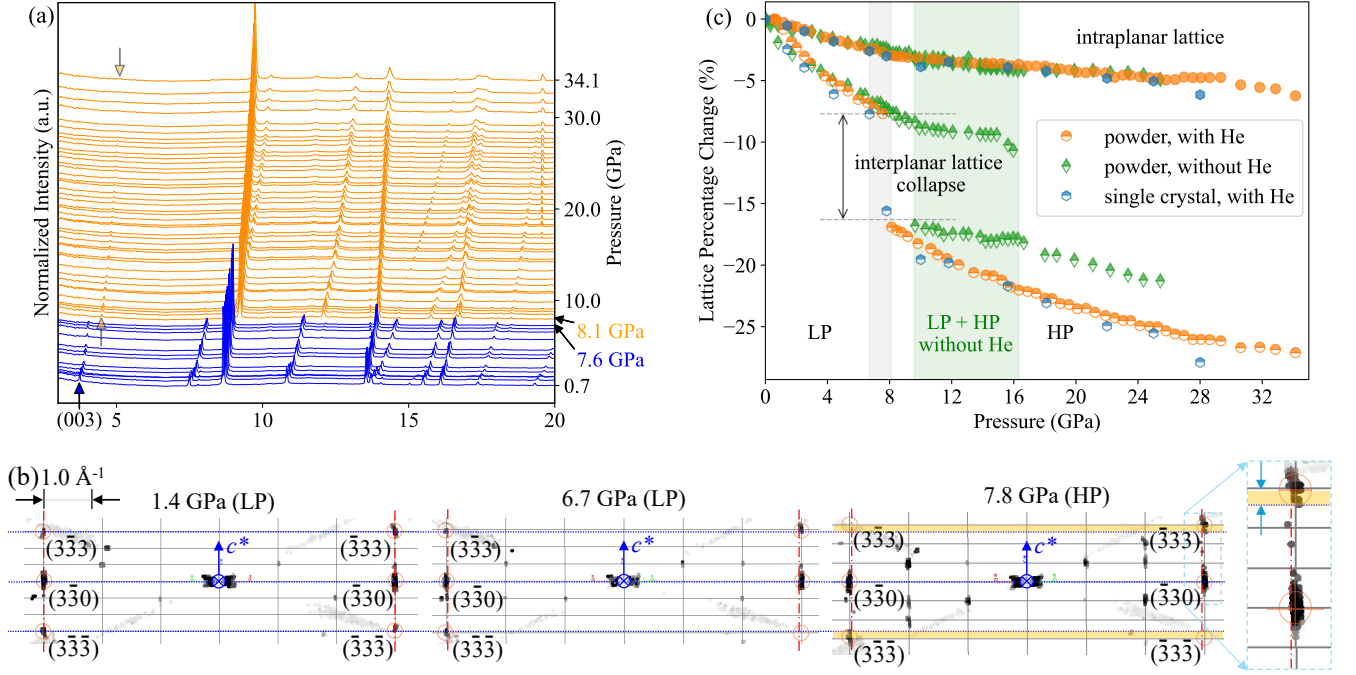


FIG. 1. (a) Integrated diffraction intensities as a function of 2θ for FePSe_3 powder sample in a DAC loaded with helium gas as a pressure-transmitting medium (PTM). For each pressure, the intensity was normalized to its maximum, and then an offset proportional to pressure values was added. Blue and orange represent data assigned to the LP and HP phases, respectively. (b) Slices of $(hh0)$ planes at the lowest pressure (1.4 GPa, LP), before (6.7 GPa, LP) and after (7.8 GPa, LP) the phase transition pressure. The sub-pictures are all scaled in \AA^{-1} . The red and blue lines are given to guide the eye to show the separation distance at the 1.4 GPa, LP phase. The yellow color blocks highlight the difference in the separation of c^* . A zoom-in view is provided at 7.8 GPa to better illustrate the abrupt changes in c^* . (c) Pressure-induced relative changes of the lattice parameters in reference to the ambient-pressure structure. Orange, green and blue represent different experimental setups. The grey-shaded region indicates the interplanar lattice collapse transition pressure. The green-shaded region represents the coexistence of LP and HP phases in the absence of a PTM.

parameters as a function of pressure, resulting from our comprehensive synchrotron studies. It can be seen that the intraplanar lattice parameters decrease smoothly at an average rate of $\sim 0.17\%$ per GPa. The interplanar distance, by contrast, declines more rapidly at an average rate of $\sim 0.86\%$ per GPa, followed by an abrupt drop of $8 \sim 10\%$ across the LP-HP transition. After the transition, c continues to decrease at a rate of $\sim 0.50\%$ per GPa up to the highest pressure. The LP-HP transition region is shaded to guide the eye. In the absence of helium gas as a PTM, the LP-HP transition and c collapse occurred at higher pressures and experienced a wide co-existence region before transforming into a pure HP phase above 16.3 GPa.

Full atomic information was obtained by a qualitative analysis of the high-pressure single-crystal data, defining the description of the space group. Data below 6.7 GPa were well-refined with the LP structure model of the $R\bar{3}$ space group. Refinements of the data above 7.8 GPa with the $R\bar{3}$ space group gave poor quality parameters. Careful inspection showed the presence of extra Bragg peaks due to a lower symmetry, and could all be indexed and refined with the $R3$ space group. Two representa-

tive sets of crystallographic information for the LP and HP phases, including refinement parameters, are given in Table III. The atomic position information is given in the SM [30]. The solved $R3$ model of the HP phase can be equally successfully used to refine powder data.

TABLE III. Reduced crystallographic data of single-crystal FePSe_3 at 4.4 GPa and 10.0 GPa from the single-crystal X-ray diffraction experiment. Here we use the primitive hexagon cell description for the lattice parameters.

| | | 4.4 GPa | 10.0 GPa |
|-----------------------|---------------------------|------------|------------|
| Lattice parameters | Space group | $R\bar{3}$ | $R3$ |
| | $a = b$ (\AA) | 6.0971(6) | 6.0155(7) |
| | c (\AA) | 18.279(19) | 15.34(6) |
| | Volume (\AA^3) | 588.5 (6) | 480.8 (18) |
| Refinement parameters | $R[F^2 > 2\sigma(F^2)]$ | 0.0038 | 0.090 |
| | $wR(F^2)$ | 0.095 | 0.221 |
| | S | 0.88 | 2.1 |
| | Reflections | 36 | 125 |

Fig. 2 exhibits the crystalline structure of LP and HP FePSe_3 side by side. (a) and (d) provide an isometric

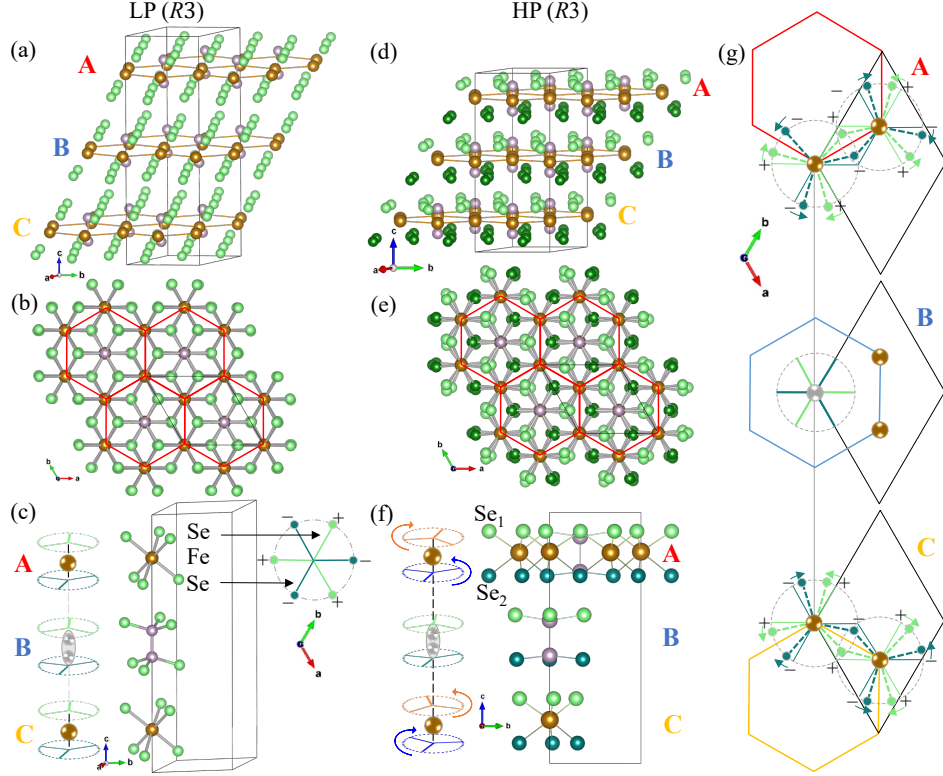


FIG. 2. Crystalline structures of the ambient-/low-pressure (LP) and high-pressure (HP) phases of FePSe₃. Fe: brown; P: grey; Se: green. (a, b) are the structural isometric view with a minimal stacking unit of ABC triple layers; (b, e) display the view normal to the vdW planes, with the red solid lines indicating the Fe-honeycomb network; (c, f) present the FeSe₆ and P₂Se₆ octahedra along the axis parallel to c . The cartoon aside depicts Se planes in both phases. The light green and dark green with + and - signs represent the Se atoms in the plane above or below the plane defined by Fe or P₂ dimer within each vdW layer. The collective displacement of Se atoms in the HP phase is demonstrated with different colors and arrows. (g) shows the normal view of the three individual stacking layers in ABC ordering. The collective rotation of each Se plane is indicated with arrows in different colors.

view of the bulk structures. Fe, P and Se atoms are shown in brown, grey and green respectively. We represent the Fe-hexagon network with solid brown lines. The interplanar distances shrink substantially from LP to HP, while the stacking geometry $ABCABC$ remains unchanged. Normal to the vdW layers, as shown in (b) and (e), the Fe-hexagon network remains undistorted from LP to HP. The $C3$ rotation symmetry is thus preserved across the transition.

The HP phase differs from the LP phase primarily in loss of the inversion symmetry, resulting from the buckling of Fe-hexagon along the c -axis and the collective displacement of Se. The LP phase only possesses one type of Wyckoff site for Se (18f), thus forming perfect octahedral coordination with Fe or P₂ positioned in the centre, as is shown in Fig. 2 (c). Within each vdW layer, Fe atoms and the centre of the P₂ dimers define one plane at z ($z = \frac{1}{6} + \frac{n}{3}$, n : integral). Se atoms at $z \pm \Delta$ positions form two sandwiching planes, represented by light and dark green colors together with + and - signs for $z + \Delta$ and $z - \Delta$, respectively. We also show a normal view to the ab plane of one Se-octahedron on the top-

right corner of Fig. 2 (c). The bonds between Fe or P₂ and the three Se atoms at the same plane ($z + \Delta$ or $z - \Delta$) are shown by contrasting colors.

In the HP phase, we observe that the Fe planes buckle slightly, resulting from Fe₁(3a) moving upward while Fe₂(3a) moving downward by $\sim 1\%$ in lattice unit along the c -axis, in reference to their center position. The Se atoms also split into two distinct Wyckoff sites, Se₁ (9b) forming one Se plane and Se₂ (9b) forming the other, as highlighted in Fig. 2 (d-f) by light and dark green colors respectively. The relative displacement of the two Se planes to the center of the Fe plane differs slightly. Within each [FeSe₆] octahedron, Se₁ and Se₂ are rotated coherently within the plane but in opposite directions between the planes. Meanwhile, the [P₂Se₆] octahedron remains nearly undistorted. We indicate the local in-plane collective rotations of Se atoms with orange and blue along one axis parallel to the c -axis in Fig. 2 (f). In addition, Fig. 2 (g) exhibits how the octahedron's local distortion propagates within and across the vdW planes in a bulk structure. We use red, blue and gold hexagon networks to present the Fe-hexagon in ABC stacking se-

quence. It can be seen that each neighboring Se-triangle rotates in the opposite direction within one Se plane. These structural distortions break the inversion symmetry of the crystalline structure, leaving FePSe₃ HP phase in the $R3$ space group with a polar point group 3, and also contribute to a net dipole moment along the c -axis.

B. Neutron Scattering and Magnetic Properties

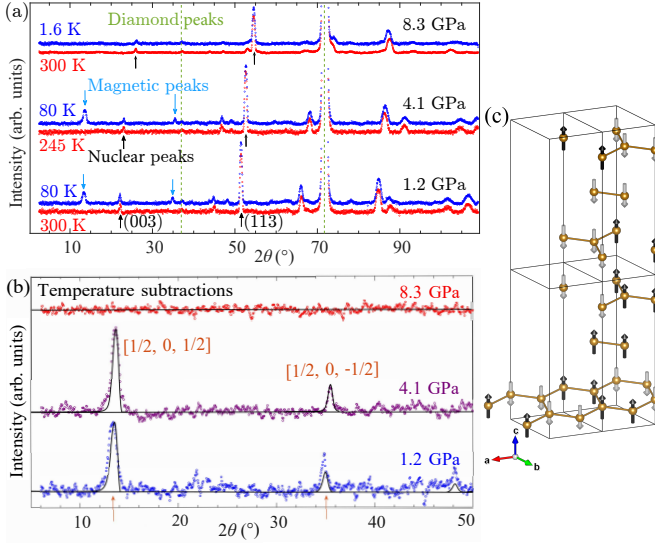


FIG. 3. Neutron powder diffraction patterns under pressures. (a) Diffraction data taken at temperatures well above (red) and below (blue) the magnetic transition temperature at pressures of 1.2, 4.1 and 8.3 GPa after background subtraction. Nuclear, magnetic peaks for FePSe₃, and peaks originating from the diamond anvils are indicated with black, cyan and green, respectively. (b) Resulting diffraction intensity obtained by subtracting the intensity at high temperature (red) from that at low temperature (blue) for each pressure point. Magnetic peaks consistent with the ambient-pressure $[\frac{1}{2}, 0, \pm\frac{1}{2}]$ magnetic propagation vectors are marked with orange arrows. Solid black lines represent refinements of the data. (c) Magnetic ordering of Fe atoms in the LP phase with the nuclear unit cell in solid black lines as a reference. The black and white arrows on Fe²⁺ atoms show opposing spin moments, parallel to the c -axis.

Fig. 3 (a) shows the neutron diffraction patterns after background subtraction at temperatures above (HT) and below (LT) the magnetic transition in red and blue respectively, for pressure values of 1.2, 4.1 and 8.3 GPa. In addition to the sample signals, there were visible peaks originating from the diamond anvils, as marked with green dotted lines in the graph. More details about background subtraction and diamond peak identification can be found in the SM [30].

The HT data (red) contained only the nuclear peaks. The indexed crystal structures were consistent with our synchrotron results. The pressure values for the neutron

measurements were then determined using the structure parameters resulting from the synchrotron data. The LT data (blue) included both nuclear and magnetic peaks. Since the nuclear peaks remained nearly unchanged with varying temperatures at each pressure point, we subtracted the HT data from the LT data to separate the magnetic peaks. The resulting temperature subtractions are shown in Fig. 3 (b).

At 1.2 and 4.1 GPa, pressures below the LP to HP crystalline transition, magnetic peaks can be seen clearly and well-indexed with the ambient-pressure magnetic structure model by Wiedenmann *et al.* [12] assuming no substantial changes in magnetic structures. The Bragg peaks corresponding to the $[\frac{1}{2}0\frac{1}{2}]$ and $[\frac{1}{2}0\frac{1}{2}]$ antiferromagnetic propagation k -vectors are marked in Fig. 3 (b).

The magnetic unit cell doubles along a and c compared to the nuclear one, as is shown in Fig. 3 (c). Only Fe²⁺ atoms with opposing spin moments in black and white arrows are shown. The nuclear unit cell is displayed with solid black lines as a reference. We demonstrate the vdW layer in the bottom layer while only showing the magnetic atoms within one cell for the remaining layers. The moment direction is normal to the ab plane, consistent with the ambient-pressure data. The FM zigzag chains are along the b direction, and are coupled with one another antiferromagnetically within the plane.

Data at a constant counting time were also collected while warming from the base temperature. We were thus able to extract the temperature dependence of the magnetic peak intensity at each pressure. At 1.2 GPa, the intensity evolution was fitted to a honeycomb-lattice 2D Ising model [44, 45], with S set to 2. This fit yields an estimated Néel temperature T_N of approximately 128 K (details in the SM [30]), slightly higher than the previously reported value of 108 ~ 119 K at ambient pressure [12, 26]. Data at 4.1 GPa were too sparse for a meaningful fit but still consistent with the trend of increased magnetic transition temperature with elevating pressure.

The magnetic moment resulting from refinements was about 3.8(2) μ_B , parallel to the c -axis, lower than that reported in Ref. [12] ($m_0 = 4.9 \mu_B$). But we recognize potential large additional uncertainty due to the role of asymmetry parameters on peak intensities.

At 8.3 GPa, at which point the nuclear structure has already changed to the HP phase with $R3$ symmetry, there was no signature of any magnetic ordering at low temperatures, down to 1.6 K. Calculating the magnitude of scattering expected from typical Fe moments and comparing with the size of signal observed in our previous FePS₃ work [36], we can be confident that any signal would be visible above the level of noise in the data.

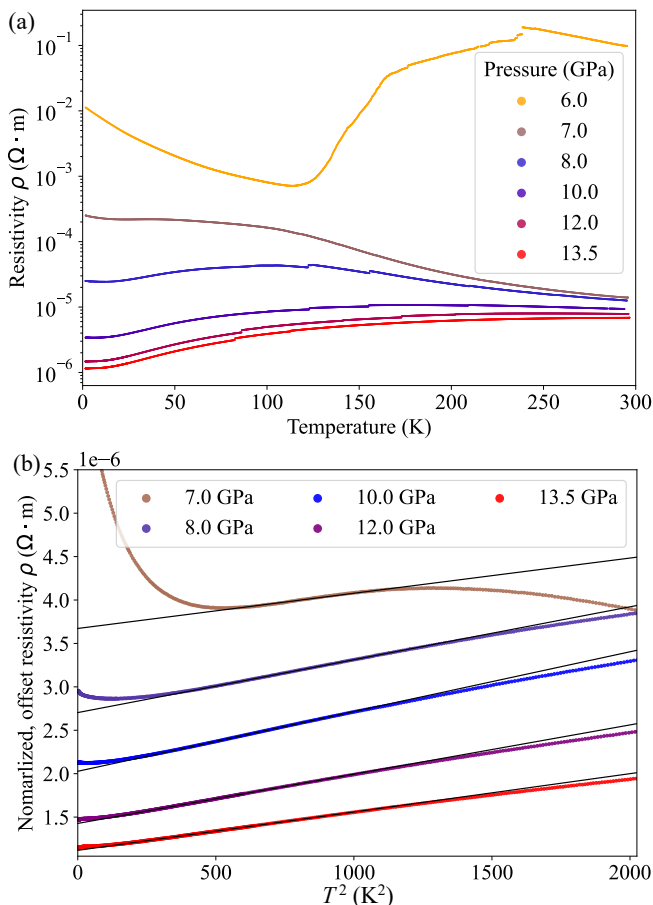


FIG. 4. (a) The resistivity ρ of a FePSe₃ single crystal, loaded in a Cubic Anvil Cell with glycerin as the pressure-transmitting medium. (b) Normalized and offset resistivity as a function of T^2 , a Fermi-liquid temperature power law, below ~ 40 K for FePSe₃. The fitted curves are plotted in solid black lines. The bounds of the best-fitting T^2 region for each pressure are detailed in the SM [30].

C. Transport Measurements and Electronic Properties

Fig. 4 (a) presents the temperature dependence of resistivity for a single-crystal FePSe₃ from 6.0 up to 13.5 GPa. The magnitude of the resistivity decreased by four orders of magnitude at room temperature from 6.0 to 7.0 GPa, indicating an insulator-to-metal transition (IMT).

At 6.0 GPa, FePSe₃ still shows insulating behavior. In the high-temperature region ($T > 250$ K), where the conduction is dominated by thermally activated behavior, the data can be well-described by an Arrhenius-type exponential expression, $\rho(T) \sim e^{E_a/(k_B T)}$. Plotting $\ln(\rho)$ against $1/T$ allows us to perform a polynomial fit, which yields an extracted activation energy E_a of around 0.08 eV. Polynomial fitting details are given in the SM [30].

In lower temperature region of the 6.0 GPa data, the

resistivity gradient shows abnormal changes at around 124 K with a broad and flat peak, which could potentially result from underlying magnetic transitions. Further analysis and repeated thermal cycling would be needed to uncover more details.

At the onset of the conducting phase, in the 7.0, 8.0, and 10.0 GPa data, we find that the resistivity increases, initially upon cooling from 300 K, similar to the activated behavior of an insulator or semiconductor. Upon additional cooling, the resistivity shows a broad maximum at approximately 40, 100, and 190 K for the 7.0, 8.0, and 10.0 GPa data respectively, before the resistivity decreases upon further cooling as expected in a metal. At the two highest pressure points, 12.0 and 13.5 GPa, such a trend was not discernible within the measured temperature range. The resistivity decreases upon cooling from 300 K.

Further analysis of the conducting phase finds that FePSe₃ exhibits a region of Fermi-liquid $\rho(T) \sim T^2$ behavior at temperatures below ~ 40 K, as shown in Fig. 4 (b). We identify this as the signature of being a “good” metal. The T^2 fits are detailed in the SM [30].

This behavior, however, terminates with an upturn in the resistivity at even lower temperatures (< 15 K). The low-temperature resistivity upturn is observed around 20 K, 10 K and 6 K in the 7.0, 8.0 and 10.0 GPa data, respectively. It is quickly suppressed with elevated pressure, becoming completely absent above 10.0 GPa.

We did not observe superconductivity in our FePSe₃ single-crystal sample for pressures up to 13.5 GPa and temperatures down to 1.6 K, in contrast to Wang *et al.* observing above 8 GPa SC with a T_c of 2.5 K [13]. Our crystallographic data showed our sample to be of good crystalline quality and the structural model to be correctly interpreted. The cubic anvil cell provided highly hydrostatic pressure conditions, and measurement currents were kept low ($< 10 \mu\text{A}$), thus ruling out the most common extrinsic reasons for not observing a superconducting phase. Yet we did observe a small ($\sim 1\%$ of $\rho(T \rightarrow 0)$) decrease in the resistivity around 3 K at 10.0 GPa which rises to around 4 K at 13.5 GPa. We also note that elemental Se [46, 47], Fe [48] and FeSe [49] have been reported to turn SC at coincidentally comparable values to those reported by Wang *et al.*. More arguments can be found in the SM [30].

IV. DISCUSSION

Drawing together our results from multiple experimental probes, we present a comprehensive temperature-pressure phase diagram for FePSe₃ in Fig. 5. The color blocks represent different phases, with gradient-shaded boundaries to guide the eye.

Our comprehensive synchrotron studies establish that FePSe₃ at 300 K undergoes a $R\bar{3}$ (LP) to $R3$ (HP) structural transition at approximately 7–8 GPa with the application of external hydrostatic pressure. A significant

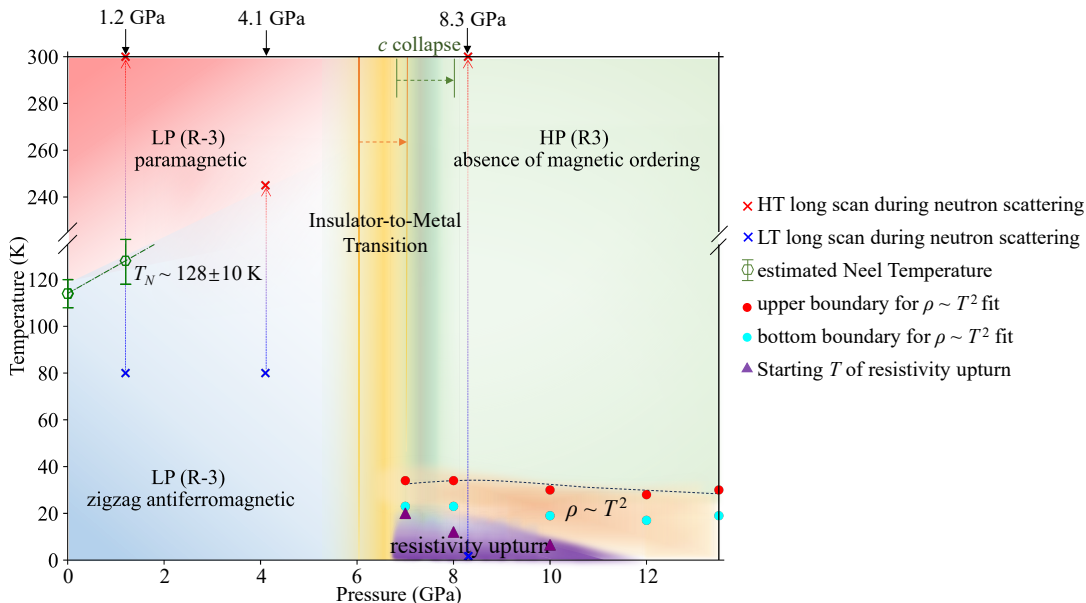


FIG. 5. Phase diagram of FePSe₃. The green open circles correspond to the antiferromagnetic transition temperature. The one at ambient pressure is from literature (magnetic susceptibility measurement), and the one at 1.2 GPa is derived from the intensity versus temperature change in our neutron diffraction data (fitted curve in the supplementary). The shaded light orange region refers to where the resistivity follows the $\rho \sim T^2$ behavior with the upper boundary in red, and the lower boundary in cyan. The region under the purple triangles is where the resistivity upturn was observed.

interplanar collapse along the c -axis occurs during this LP-HP transition. The HP phase loses the inversion centre yet preserves the undistorted Fe-honeycomb lattice, crystallizing in the $R3$ space group.

Our powder neutron diffraction studies under pressure affirm that the LP phase experiences a paramagnetic to antiferromagnetic transition. The magnetic configuration of LP remains the same as that reported in the ambient-pressure model [12], with the magnetic propagation vector $[\frac{1}{2}0 \pm \frac{1}{2}]$ and the moments parallel to the c -axis. Zigzag ferromagnetic chains form within the vdW planes and couple with one another antiferromagnetically. The space group symmetry remains unchanged with varying temperature. The magnetic transition temperature tends to increase slightly with elevated pressure. In the HP phase, we did not observe any presence of magnetic ordering from 300 K to the base temperature 1.6 K.

Our resistivity measurements point out the band gap of the LP phase shrinks at 6 GPa, compared to the ambient-pressure literature value, which agrees qualitatively with the previous report [13]. We also observe an insulator-to-metal transition (IMT) from 6 to 7 GPa in FePSe₃, as marked with the yellow dotted arrow in Fig. 5. The IMT transition pressure corresponds to the LP-HP structural transition pressure.

At higher pressures in the HP phase, FePSe₃ behaves as a “good” metal following $\rho \sim T^2$ Fermi-liquid descriptions below ~ 40 K. The fitted boundary of this temperature-pressure region is marked with dots in Fig. 5. An upturn in the resistivity, deviating from this state, emerges at even lower temperatures, marked with

purple. Such deviation is more discernible in proximity to the AFM transition and is fully suppressed at 12 GPa. No bulk superconductivity was observed in the HP phase up to the highest pressure (13.5 GPa) during the measurement.

A. Loss of inversion-symmetry and Interplanar Collapse

We note that our LP-HP transition model contrasts with the intraplanar lattice collapse model previously proposed by Wang *et al.* [13]. We cannot comment on the contradictory interpretations but would rather draw attention to the different experimental setups. Wang *et al.* used pre-compressed FePSe₃ pellets and silicone oil as a PTM for data collection. In this paper, we used powder samples from growth and high-quality single crystals both loaded with helium gas as a PTM. Our single-crystal measurements give model-independent proof through the (hhl) plane slices that an interplanar collapse occurred during the LP-HP transition. The powder samples, regardless of the presence of a PTM, also supports the c -collapse in the HP phase and verifies the HP structural model, involving the loss of the inversion symmetry, as obtained from the single-crystal data. We thus confidently affirm our LP-HP structural transition model.

We would also like to underline the point that it is critical to ensure a hydrostatic pressure medium during sample loading and pressurizing, considering the nature of vdW layered compounds. Strongly preferred orienta-

tion in powder samples or stacking faults in single crystals could potentially impact the observed results. Similar cases have been previously reported in this compound family, such as in NiPS_3 [25]. We utilized helium as it has been documented to be the best available PTM, even in its solid state above ~ 12.1 GPa [50]. We found that, in the absence of a PTM, the onset of the LP-HP structural transition was observed at a higher pressure value (~ 9.6 GPa), and was followed by a co-existence region of both LP and HP till 16.3 GPa. A pure HP phase was not evident before this pressure value.

B. Suppression of Magnetic Ordering

We find that the magnetic configuration of LP is consistent with the ambient-pressure model [12], while the size of the magnetic moments shrinks with increased pressure. Additionally, the value of T_N tends to increase with elevated pressure. We note that the interplanar distance shrinks more rapidly than the intraplanar atomic separation in the LP phase, which might affect the coordination around the magnetic fragments subtly. Further explorations, for instance, magnetic susceptibility measurements, neutron inelastic scattering under pressure or magnetic exchange interaction simulations, would be needed to gain full understanding into the magnetic phase transitions.

After the structural transition in the HP phase, however, no magnetic peaks or short-range-ordering features are visible in our neutron powder diffraction data. We thus conclude that FePSe_3 does not order magnetically in the HP phase, in interesting contrast to the sulfur compound FePS_3 [36]. The system may experience a reconfiguration of electronic states as FePSe_3 becomes more three-dimensional (3D) and carriers become itinerant after the LP-HP transition. The absence of magnetic ordering at HP might be due to a spin crossover from a high-spin moment state ($S = 2$) to a zero-magnetic-moment state ($S = 0$) as observed by Wang *et al.* [13].

C. Novel Metallic Phases

We identify that FePSe_3 undergoes an IMT concomitant with the LP-HP structural transition. One aspect is that the associated interplanar c -collapse coincides with the IMT. Similar features were reported in MnPS_3 , FePS_3 and NiPS_3 previously [4, 14, 19], but should not be considered as universal across this family, as recent cases of VPS_3 [51] and NiPSe_3 [15] manifest contradictory behaviors.

The more essential aspect is that FePSe_3 could be a polar metal at accessible pressures. We identify the broken inversion symmetry and a polar point group symmetry from the synchrotron diffraction data. The detailed analysis of the atomic displacement suggests that a net dipole moment could exist locally in the HP phase. Though po-

lar metals are promising multifunctional materials [9], they are limited by experimental realizations. So far there are only a few known examples in CePt_3Si [52], UIr [53], LiOsO_3 [54], WTe_2 [55], doped SrTiO_3 [7], pressurized $\text{Hg}_3\text{Te}_2\text{X}_2$ [8] and another recent candidate NiPS_3 at the rather high pressure value of 23 GPa [56]. FePSe_3 , in this case, is worthy of further explorations into the polarization and charge distributions. Our unambiguous structural model of this clean and simple system therefore lays a solid foundation for further experiments and density functional theory calculations.

In the conducting phase, from 7 GPa, we observe that the resistivity ascends towards a broad plateau (above ~ 40 K) with decreasing temperature from 300 K and the plateau moves towards a higher temperature value from 7 to 10 GPa till it exceeds our measurable temperature range at 12 GPa. This is similar to a thermally activated behavior in an insulator, but we note that the resistivity value (less than the order of $10^{-4} \Omega \cdot m$) is conducting in nature. It suggests another interesting intermediate state for further explorations.

Below ~ 40 K, we observe that the resistivity of FePSe_3 follows Fermi-liquid description. However, this state terminates with an upturn in resistivity at even lower temperatures in a pressure range of 7-10 GPa. We find this feature forms a dome in the temperature-pressure phase diagram, close to the antiferromagnetic critical transition pressure point. Similar deviations have been previously reported in other TMPS_3 materials and are still awaiting full explanations [4, 14]. More generally, the strongly correlated electrons are likely to introduce quantum critical fluctuations close to a quantum critical point associated with magnetic transitions [53, 57], leading to emergent phenomena including unconventional superconductivity or novel metallic states. Additionally, the broken inversion symmetry may yield a Rashba-type spin-orbit coupling and thus exclude the spin-triplet pairing in FePSe_3 HP phase [52]. Further investigations are needed to deepen the understanding of this non-centrosymmetric compound's novel phases and underlying mechanism.

V. CONCLUSIONS

To conclude, the van-der-Waals compound FePSe_3 is a Mott-insulator with antiferromagnetic ordering at ambient pressure, providing a rich platform to explore the full tuning of an insulator into novel metallic states via the application of pressure.

We identify a crystalline transition from the centrosymmetric $R\bar{3}$ to the non-centrosymmetric $R3$ space group at approximately 7 GPa through rigorous synchrotron diffraction studies. This transition is accompanied by a substantial interplanar lattice collapse with no evidence of interplanar sliding. More essentially, the local distortion of Se atoms and the buckling of the Fe atoms result in the loss of inversion symmetry and the formation of net dipole moments along the c -axis.

We also observe the suppression of magnetic ordering and an insulator-to-metal transition at a correspondent transition pressure. As a result, we report the emergence of a polar metal phase in FePSe_3 at accessible pressures, which offers a chemically simple and clean system to explore polar metallicity beyond the limited experimental realizations to date. Additionally, the resistivity deviates from Fermi-liquid behavior in the pressure range of $7 \sim 10$ GPa at sufficiently low temperatures. This abnormality, appearing only close to the magnetic critical transition pressure, strongly suggests the underlying new quantum ordering, necessitating further explorations.

Overall, our multi-probe studies of the crystalline, magnetic structures and transport properties of FePSe_3 contribute significantly to the intrinsic understanding of the TMPX_3 compound family. Despite extensive studies of macroscopic physical properties, this work presents the first fundamental understanding of structures in relation to the emergent novel metallic phases. These findings offers a solid starting point for further physical properties investigations and *ab-initio* studies. Further study, involving the control of individual layers and stacking patterns, will also be an area of interest for advancing the engineering of low-dimensional magnetism in van-der-Waals materials and applying them into atomically thin-layer device architectures.

VI. ACKNOWLEDGMENT

Funding Information This project has received funding from the U.K. Department of Science, Innovation and Technologies (DSIT), Grants No.G115693, to support collaboration between the Cavendish Laboratory and the Navoi State University of Mining and Technologies. SD acknowledges Cambridge Trust, WP Napier PhD Studentship, Cambridge Philosophical Society Research Studentships for pursuing doctoral study and the ILL Theory group support for continuing the work. The work at SNU (CK, JGP) is funded by the Leading Researcher Program of the National Research Foundation of Korea (Grant No. 2020R1A3B2079375). PTY, BSW and JGC are supported by the National Key Research and Development Program of China (2023YFA1406100, 2023YFA1607400), National Natural Science Foundation of China (12025408, 11921004, U23A6003, 12474055, 12404067) and the outstanding member of Youth Promotion Association of CAS (Y2022004). We also acknowledge the meaningful discussions with Emilio Artacho and Patricia L. Alireza.

Facility Time The synchrotron X-ray experiments were carried out with the support of the Diamond Light Source through the approved beamtime proposals CY31687-1 on I19-2 and CY31687-2 on I15. The neutron scattering experiment was performed with the support of the Institut Laue-Langevin, Grenoble, France through the approval of beamtime for proposal 5-31-2847 (DOI: 10.5291/ILL-DATA.5-31-2847) [35]. The resistivity measurements were conducted at the Cubic Anvil Cell Station of the Synergetic Extreme Condition User Facility (SECUF).

-
- [1] Y. Zhang, Y.-W. Tan, H. L. Stormer, and P. Kim, Experimental observation of the quantum hall effect and berry's phase in graphene, *Nature* **438**, 201 (2005).
 - [2] J. G. Park, Opportunities and challenges of 2D magnetic van der Waals materials: magnetic graphene?, *J. Condens. Matter Phys.* **28**, 301001 (2016).
 - [3] Q. H. Wang, A. Bedoya-Pinto, M. Blei, A. H. Dismukes, A. Hamo, S. Jenkins, M. Koperski, Y. Liu, Q.-C. Sun, E. J. Telford, H. H. Kim, M. Augustin, U. Vool, J.-X. Yin, L. H. Li, A. Falin, C. R. Dean, F. Casanova, R. F. L. Evans, M. Chshiev, A. Mishchenko, C. Petrovic, R. He, L. Zhao, A. W. Tsen, B. D. Gerardot, M. Brotons-Gisbert, Z. Guguchia, X. Roy, S. Tongay, Z. Wang, M. Z. Hasan, J. Wrachtrup, A. Yacoby, A. Fert, S. Parkin, K. S. Novoselov, P. Dai, L. Balicas, and E. J. G. Santos, The magnetic genome of two-dimensional van der waals materials, *ACS Nano* **16**, 6960 (2022).
 - [4] C. R. S. Haines, M. J. Coak, A. R. Wildes, G. I. Lampronti, C. Liu, P. Nahai-Williamson, H. Hamidov, D. Daisenberger, and S. Saxena, Pressure-Induced Electronic and Structural Phase Evolution in the van der Waals Compound FePS_3 , *Phys. Rev. Lett.* **121**, 266801 (2018).
 - [5] J. G. Bednorz and K. A. Müller, Possible high T_c superconductivity in the Ba-La-Cu-O system, *Zeitschrift für Phys. B Condens. Matter* **64**, 189 (1986).
 - [6] Z. Z. Sheng and A. M. Hermann, Bulk superconductivity at 120 K in the Tl-Ca/Ba-Cu-O system, *Nature* **332**, 138 (1988).
 - [7] C. Enderlein, J. F. de Oliveira, D. A. Tompsett, E. B. Saitovitch, S. S. Saxena, G. G. Lonzarich, and S. E. Rowley, Superconductivity mediated by polar modes in ferroelectric metals, *Nat. Commun.* **11**, 4852 (2020).
 - [8] W. Cai, J. He, H. Li, R. Zhang, D. Zhang, D. Y. Chung, T. Bhowmick, C. Wolverton, M. G. Kanatzidis, and S. Deemyad, Pressure-induced ferroelectric-like transition creates a polar metal in defect antiperovskites $\text{Hg}_3\text{Te}_2\text{X}_2$ ($\text{X} = \text{Cl}, \text{Br}$), *Nat. Commun.* **12**, 1509 (2021).
 - [9] D. Hickox-Young, D. Puggioni, and J. M. Rondinelli, Polar metals taxonomy for materials classification and discovery, *Phys. Rev. Mater.* **7**, 010301 (2023).
 - [10] W. Klingens, G. Eulenberger, and H. Hahn, Über die kristallstrukturen von $\text{Fe}_2\text{P}_2\text{Se}_6$ und $\text{Fe}_2\text{P}_2\text{S}_6$, *Z. für Anorg. Allg. Chem.* **401**, 97 (1973).
 - [11] R. Brec, D. M. Schleich, G. Ouvrard, A. Louisy, and J. Rouxel, Physical properties of lithium inter-

- calation compounds of the layered transition-metal chalcogenophosphites, *Inorg. Chem.* **18**, 1814 (1979).
- [12] A. Wiedenmann, J. Rossat-Mignod, A. Louisy, R. Brec, and J. Rouxel, Neutron diffraction study of the layered compounds MnPSe_3 and FePSe_3 , *Solid State Commun.* **40**, 1067 (1981).
- [13] Y. Wang, J. Ying, Z. Zhou, J. Sun, T. Wen, Y. Zhou, N. Li, Q. Zhang, F. Han, Y. Xiao, P. Chow, W. Yang, V. V. Struzhkin, Y. Zhao, and H. Mao, Emergent superconductivity in an iron-based honeycomb lattice initiated by pressure-driven spin-crossover, *Nat. Comm.* **9**, 1914 (2018).
- [14] M. J. Coak, D. M. Jarvis, H. Hamidov, C. R. S. Haines, P. L. Alireza, C. Liu, S. Son, I. Hwang, G. I. Lampronti, D. Daisenberger, P. Nahai-Williamson, A. R. Wildes, S. S. Saxena, and J. G. Park, Tuning dimensionality in van-der-Waals antiferromagnetic Mott insulators TMPS_3 , *J. Phys. Condens. Matter* **32**, 124003 (2020).
- [15] H. Sun, L. Qiu, Y. Han, E. Yi, J. Li, M. Huo, C. Huang, H. Liu, M. Li, W. Wang, D. Yao, B. A. Frandsen, B. Shen, Y. Hou, and M. Wang, Coexistence of zigzag antiferromagnetic order and superconductivity in compressed NiPS_3 , *Mater. Today Phys.* **36**, 101188 (2023).
- [16] B. Yue, W. Zhong, T. Wen, Y. Wang, H. Yu, X. Yu, C. Chen, J.-T. Wang, and F. Hong, Pressure-induced ferroelectric-to-superconductor transition in SnPS_3 , *Phys. Rev. B* **107**, L140501 (2023).
- [17] M. Qi, W. Chen, Y. Huang, H. Song, X. Lv, M. Wu, W. Zhao, L. Zhang, and T. Cui, Pressure-induced superconductivity in van der waals layered semiconductor snps_3 , *J. Mater. Chem. C* **12**, 5108 (2024).
- [18] C. Li, Y. Wang, K. Liu, D. Jiang, J. Feng, T. Wen, B. Yue, Y. Zhou, L. Sun, and Y. Wang, Superconductivity in Quasi-One-Dimensional Ferromagnet CrSbSe_3 under High Pressure, *J. Am. Chem. Soc.* **146**, 9688 (2024).
- [19] X. Ma, Y. Wang, Y. Yin, B. Yue, J. Dai, J. Cheng, J. Ji, F. Jin, F. Hong, J. T. Wang, Q. Zhang, and X. Yu, Dimensional crossover tuned by pressure in layered magnetic NiPS_3 , *Sci. China: Phys. Mech. Astron.* **64**, 1 (2021).
- [20] D. M. Jarvis, M. J. Coak, H. Hamidov, C. R. S. Haines, G. I. Lampronti, C. Liu, S. Deng, D. Daisenberger, D. R. Allan, M. R. Warren, A. R. Wildes, and S. S. Saxena, Comparative structural evolution under pressure of powder and single crystals of the layered antiferromagnet FePS_3 , *Phys. Rev. B* **107**, 54106 (2023).
- [21] C. T. Kuo, M. Neumann, K. Balamurugan, H. J. Park, S. Kang, H. W. Shiu, J. H. Kang, B. H. Hong, M. Han, T. W. Noh, and J. G. Park, Exfoliation and Raman Spectroscopic Fingerprint of Few-Layer NiPS_3 Van der Waals Crystals, *Sci. Rep.* **6**, 20904 (2016).
- [22] X. Wang, K. Du, F. L. Y., P. Hu, J. Zhang, Q. Zhang, M. H. S. Owen, X. Lu, C. K. Gan, P. Sengupta, C. Kloc, and Q. Xiong, Raman spectroscopy of atomically thin two-dimensional magnetic iron phosphorus trisulfide (FePS_3) crystals, *2D Materials* **3**, 031009 (2016).
- [23] K. Du, X. Wang, Y. Liu, P. Hu, M. I. B. Utama, C. K. Gan, Q. Xiong, and C. Kloc, Weak Van der Waals Stacking, Wide-Range Band Gap, and Raman Study on Ultrathin Layers of Metal Phosphorus Trichalcogenides, *ACS Nano* **10**, 1738 (2016).
- [24] S. Das, S. Chaturvedi, D. Tripathy, S. Grover, R. Singh, D. Muthu, S. Sampath, U. Waghmare, and A. Sood, Raman and first-principles study of the pressure-induced Mott-insulator to metal transition in bulk FePS_3 , *J. Phys. Chem. Solids* **164**, 110607 (2022).
- [25] T. Matsuoka, H.-S. Kim, S. Samanta, J. L. Musfeldt, and D. Mandrus, MPX_3 van der Waals magnets under pressure ($M = \text{Mn, Ni, V, Fe, Co, Cd}$; $X = \text{S, Se}$), *Front. Mater.* **11**, 1362744 (2024).
- [26] Q. Xie, S. Hu, C. Hu, Q. Sheng, L. Chen, J. Zheng, W. Wang, L. Ma, and G. Cheng, Identification of phonon symmetry and spin-phonon coupling in van der Waals antiferromagnetic FePS_3 , *Appl. Phys. Lett.* **122**, 161901 (2023).
- [27] J. Filik, A. Ashton, P. Chang, P. Chater, S. Day, M. Drakopoulos, M. Gerring, M. Hart, O. Magdysyuk, S. Michalik, *et al.*, Processing two-dimensional X-ray diffraction and small-angle scattering data in DAWN 2, *J. Appl. Cryst.* **50**, 959 (2017).
- [28] B. H. Toby and R. B. Von Dreele, GSAS-II: the genesis of a modern open-source all purpose crystallography software package, *J. Appl. Cryst.* **46**, 544 (2013).
- [29] H. Nowell, S. A. Barnett, K. E. Christensen, S. J. Teat, and D. R. Allan, I19, the small-molecule single-crystal diffraction beamline at Diamond Light Source, *J. Synchrotron Radiat.* **19**, 435 (2012).
- [30] See Supplemental Material at URL-will-be-inserted-by-publisher for full details of the experimental measurements and data processing.
- [31] Agilent Technologies UK Ltd., Oxford, UK, *CrysAlis Pro* (2014).
- [32] H. K. Mao, J. Xu, and P. M. Bell, Calibration of the ruby pressure gauge to 800 kbar under quasi-hydrostatic conditions, *J. Geophys.* **91**, 4673 (1986).
- [33] G. Shen, Y. Wang, A. Dewaele, C. Wu, D. E. Fratanduono, J. Eggert, S. Klotz, K. F. Dziubek, P. Loubeyre, O. V. Fatyanov, P. D. Asimow, T. Mashimo, and R. M. M. Wentzcovitch, Toward an international practical pressure scale: A proposal for an IPPS ruby gauge (IPPS-Ruby2020), *High Press. Res.* **40**, 299 (2020).
- [34] T. C. Hansen, P. F. Henry, H. E. Fischer, J. Torregrossa, and P. Convert, The D20 instrument at the ILL: a versatile high-intensity two-axis neutron diffractometer, *Meas. Sci. Technol.* **19**, 034001 (2008).
- [35] D. M. Jarvis, M. J. Coak, S. Deng, S. E. Dutton, F. Leon, C. R. S. Haines, H. Hayrullo, T. C. Hansen, K. Stefan, L. Cheng, S. S. Siddharth, and A. R. Wildes, Evolution of magnetism in the two-dimensional antiferromagnet FePS_3 beyond pressure-induced superconductivity, Institut Laue-Langevin (ILL) [10.5291/ILL-DATA.5-31-2847](https://arxiv.org/abs/10.5291/ILL-DATA.5-31-2847) (2021).
- [36] M. J. Coak, D. M. Jarvis, H. Hamidov, A. R. Wildes, J. A. M. Paddison, C. Liu, C. R. S. Haines, N. T. Dang, S. E. Kichanov, B. N. Savenko, S. Lee, M. Kratochvílová, S. Klotz, T. C. Hansen, D. P. Kozlenko, J.-G. Park, and S. S. Saxena, Emergent Magnetic Phases in Pressure-Tuned van der Waals Antiferromagnet FePS_3 , *Phys. Rev. X* **11**, 011024 (2021).
- [37] S. Klotz, T. Strässle, G. Rousse, G. Hamel, and V. Pomjakushin, Angle-dispersive neutron diffraction under high pressure to 10 GPa, *Appl. Phys. Lett.* **86**, 031917 (2005).
- [38] S. Klotz, T. Strässle, B. Lebert, M. d'Astuto, and T. Hansen, High pressure neutron diffraction to beyond 20 GPa and below 1.8 K using Paris-Edinburgh load frames, *High Pressure Research* **36**, 73 (2016).
- [39] W. G. Marshall and D. J. Francis, Attainment

- of near-hydrostatic compression conditions using the paris–edinburgh cell, *J. Appl. Crystallogr.* **35**, 122 (2002).
- [40] G. L. M. S. Klotz, L. Paumier and P. Munsch, The effect of temperature on the hydrostatic limit of 4:1 methanol-ethanol under pressure, *High Press. Res.* **29**, 649 (2009).
- [41] J. Rodríguez-Carvajal, Fullprof, CEA/Saclay, France **1045**, 132 (2001).
- [42] J.-G. Cheng, B.-S. Wang, J.-P. Sun, and Y. Uwatoko, Cubic anvil cell apparatus for high-pressure and low-temperature physical property measurements, *Chin. Phys. B* **27**, 077403 (2018).
- [43] J.-G. Cheng, K. Matsubayashi, S. Nagasaki, A. Hisada, T. Hirayama, M. Hedo, H. Kagi, and Y. Uwatoko, Integrated-fin gasket for palm cubic-anvil high pressure apparatus, *Rev. Sci. Instrum.* **85**, 093907 (2014).
- [44] R. J. Baxter, *Exactly solved models in statistical mechanics* (Courier Corporation, 2007).
- [45] K. C. Rule, G. J. McIntyre, S. J. Kennedy, and T. J. Hicks, Single-crystal and powder neutron diffraction experiments on FePS₃: Search for the magnetic structure, *Phys. Rev. B* **76**, 134402 (2007).
- [46] F. P. Bundy and K. J. Dunn, Electrical behavior of te, se, and s at very high pressures and low temperatures: Superconduction transitions, *Phys. Rev. B* **22**, 3157 (1980).
- [47] Y. Akahama, M. Kobayashi, and H. Kawamura, Pressure-induced superconductivity and phase transition in selenium and tellurium, *Solid state communications* **84**, 803 (1992).
- [48] K. Shimizu, T. Kimura, S. Furomoto, K. Takeda, K. Kontani, Y. Onuki, and K. Amaya, Superconductivity in the non-magnetic state of iron under pressure, *Nature* **412**, 316 (2001).
- [49] F.-C. Hsu, J.-Y. Luo, K.-W. Yeh, T.-K. Chen, T.-W. Huang, P. M. Wu, Y.-C. Lee, Y.-L. Huang, Y.-Y. Chu, D.-C. Yan, *et al.*, Superconductivity in the PbO-type structure α -FeSe, *Proc. Natl. Acad. Sci.* **105**, 14262 (2008).
- [50] S. Klotz, J. C. Chervin, P. Munsch, and G. L. Marchand, Hydrostatic limits of 11 pressure transmitting media, *J. Phys. D: Appl. Phys.* **42**, 075413 (2009).
- [51] M. J. Coak, S. Son, D. Daisenberger, H. Hamidov, C. R. S. Haines, P. L. Alireza, A. R. Wildes, C. Liu, S. S. Saxena, and J.-G. Park, Isostructural Mott transition in 2D honeycomb antiferromagnet V_{0.9}PS₃, *npj Quantum Mater.* **4**, 38 (2019).
- [52] E. Bauer, G. Hilscher, H. Michor, C. Paul, E. W. Scheidt, A. Griбанov, Y. Seropegin, H. Noël, M. Sigrist, and P. Rogl, Heavy Fermion Superconductivity and Magnetic Order in Noncentrosymmetric CePt₃Si, *Phys. Rev. Lett.* **92**, 027003 (2004).
- [53] T. Akazawa, H. Hidaka, H. Kotegawa, T. C. Kobayashi, T. Fujiwara, E. Yamamoto, Y. Haga, R. Settai, and Y. Ōnuki, Pressure-induced Superconductivity in UIr, *J. Phys. Soc. Jpn.* **73**, 3129 (2004).
- [54] Y. Shi, Y. Guo, X. Wang, A. J. Princep, D. Khalyavin, P. Manuel, Y. Michiue, A. Sato, K. Tsuda, S. Yu, M. Arai, Y. Shirako, M. Akaogi, N. Wang, K. Yamaura, and A. T. Boothroyd, A ferroelectric-like structural transition in a metal, *Nat. Mater.* **12**, 1024 (2013).
- [55] P. Sharma, F. X. Xiang, D. F. Shao, D. Zhang, E. Y. Tsybal, A. R. Hamilton, and J. Seidel, A room-temperature ferroelectric semimetal, *Sci. Adv.* **5**, eaax5080 (2019).
- [56] N. C. Harms, T. Matsuoka, S. Samanta, A. J. Clune, K. A. Smith, A. V. Haglund, E. Feng, H. Cao, J. S. Smith, D. G. Mandrus, H.-S. Kim, Z. Liu, and J. L. Musfeldt, Symmetry progression and possible polar metallicity in NiPS₃ under pressure, *npj 2D Mater. Appl.* **6**, 40 (2022).
- [57] D. Belitz, T. R. Kirkpatrick, R. Narayanan, and T. Vojta, Transport anomalies and marginal-fermi-liquid effects at a quantum critical point, *Phys. Rev. Lett.* **85**, 4602 (2000).